Nanoscale

PAPER

View Article Online
View Journal | View Issue

Cite this: *Nanoscale*, 2015, **7**, 8748

Thermal replacement reaction: a novel route for synthesizing eco-friendly ZnO@γ-In_2Se_3 hetero-nanostructures by replacing cadmium with indium and their photoelectrochemical and photocatalytic performances

Zhuo Zhang, Mingi Choi, Minki Baek and Kijung Yong*

Received 12th February 2015,
Accepted 30th March 2015

DOI: 10.1039/c5nr01025j

www.rsc.org/nanoscale

A novel route called thermal replacement reaction was demonstrated for synthesizing eco-friendly ZnO@γ-In_2Se_3 hetero-structural nanowires on FTO glass by replacing the element cadmium with indium for the first time. The indium layer was coated on the surface of the ZnO nanowires beforehand, then CdSe quantum dots were deposited onto the coated indium layer, and finally the CdSe quantum dots were converted to γ-In_2Se_3 quantum dots by annealing under vacuum at 350 °C for one hour. The prepared ZnO@γ-In_2Se_3 hetero-nanostructures exhibit stable photoelectrochemical properties that can be ascribed to the protection of the In_2O_3 layer between the ZnO nanowire and γ-In_2Se_3 quantum dots and better photocatalytic performance in the wide wavelength region from 400 nm to nearly 750 nm. This strategy for preparing the ZnO@γ-In_2Se_3 hetero-nanostructures not only enriches our understanding of the single replacement reaction where the active element cadmium can be replaced with indium, but also opens a new way for the *in situ* conversion of cadmium-based to eco-friendly indium-based nano-devices.

Introduction

The single replacement reaction, also known as the substitution reaction, is an oxidation–reduction chemical reaction in which one element is replaced by another in a compound. The general reaction equation A + BC → B + AC exhibits that the replacement will most often occur if element A is more reactive than element B. Recently, the replacement reaction has become a versatile strategy for synthesizing a variety of nanostructures such as Au nanocages,[1] Ag nanocubes[2] and nanowires,[3] and Pd–Pt bimetallic nanocrystals.[4] Among all types of materials, cadmium selenide (CdSe) quantum dots (QDs) offer great opportunities for harvesting light energy in the visible region of the solar spectrum due to a very suitable band gap (1.7 eV),[5] which makes it the most important material for photoelectrochemical (PEC),[6] photocatalytic,[7] photovoltaic,[8] and other optical applications. However, due to the toxicity of Cd, it is necessary to replace Cd with eco-friendly elements for health and environmental reasons.[9] Although we can fabricate new nanostructures with a similar band gap instead of CdSe, considering that there are a large number of CdSe-based PEC and other nano-systems that have been developed as efficient photoanodes/catalysts, it is still essential for us to develop an *in situ* strategy for replacing Cd in CdSe-based nano-systems with other eco-friendly elements. For a successful replacement reaction of CdSe, the following prerequisites must be satisfied: (1) the replacing element should be non-toxic; (2) the Cd element needs to be completely converted; and (3) the PEC or other abilities such as sensitized solar cells[10,11] should not be degraded, that is the band gap of the newly synthesized selenide nanomaterial falls between 1.3 and 2.0 eV. According to the law of the replacement reaction, the non-toxic element for replacement must be more reactive than Cd such as Cu, Zn, and Ag. However, their nano-sized selenides are not suitable for photo-electronic applications. Cu_3Se_2 and CuSe have a rather large band gap of 2.37 eV and 2.0 eV, respectively.[12] ZnSe also has a very large band gap at 2.6–2.8 eV and is toxic to the environment,[13] and Ag_2Se has a decreasing band gap from 1.35 eV to 0.07 eV with an increasing size from nano- to bulk-scale.[14] Comparatively, indium selenide (In_xSe_y) can be an excellent candidate for replacing CdSe due to its non-toxicity and suitable band gap such as 1.4 eV for InSe and 1.3–1.7 eV for α-, β- and γ-In_2Se_3.[15] These advantages make nano-structural In_xSe_y play an important role for applications

Department of Chemical Engineering, POSTECH, Pohang 790-784, Korea.
E-mail: kyong@postech.ac.kr

in electrochemical[16] and photovoltaic devices.[17] Various strategies have been utilized to synthesize crystalline In_xSe_y such as chemical vapor deposition,[18] thermal evaporation,[19] molecular beam epitaxy,[20] and electrochemical atomic layer epitaxy.[21] However, there are no reports on In_xSe_y prepared *via* the chemical replacement reaction from CdSe. It is well known that indium (In) is less reactive than Cd, so it is impractical to replace Cd with In by the usual replacement reaction. Therefore, it is a big challenge for us to replace Cd in CdSe-based PEC or photocatalytic nano-devices by In.

In this study, we have demonstrated a novel route called the thermal replacement reaction for replacing Cd with In for the first time. We found that although the element Cd is more reactive than In in usual chemical reactions, the saturated vapor pressure of Cd is higher than that of In. Thus, due to preferential sublimation of Cd to In, In replaces Cd rendering the conversion of CdSe to γ-In_2Se_3 at high temperature conditions (350 °C). In addition, considering that the preparation method is well established for ZnO@CdSe QDs with high and uniform loading, the conversion of CdSe into γ-In_2Se_3 is an efficient way for producing eco-friendly ZnO@γ-In_2Se_3 hetero-nanostructures. Because the band gap of γ-In_2Se_3 is 1.7 eV and their band-alignment with ZnO forms a type-II band structure, it is expected that the ZnO@γ-In_2Se_3 hetero-nanostructure nanowires will be effective photocatalysts in PEC and photodecomposition reactions.

Experimental

Materials and preparations

(1) ZnO nanowires (NWs): arrays of ZnO NWs were grown on FTO glass using a seed-assisted hydrothermal method. First, the ZnO seed layer was adhered smoothly on the native FTO glass with the aid of radio frequency (RF) magnetron sputtering for 5 min under argon protection. Then, the seeded FTO glass was dipped into a mixed electrolyte consisting of hexamethylenetetramine (HTMA, 20 mM) and zinc nitrate hexahydrate [$Zn(NO_3)_2{\cdot}6H_2O$, 20 mM]. A typical deposition was continued for 12 h at 95 °C. (2) In-coated ZnO NWs: An In layer was coated on the surface of the ZnO NWs by RF magnetron sputtering for 30 seconds under argon protection. (3) CdSe QDs: CdSe QDs were deposited onto the In-coated ZnO NWs *via* chemical bath deposition (CBD), which was carried out by immersing the FTO glass with In-coated ZnO NWs into an aqueous solution consisting of $Cd(CH_3COO)_2$ (2.5 mM), Na_2SeSO_3 (2.5 mM), and NH_4OH (45 mM). A typical deposition time for the CdSe QDs was 4 h at 95 °C. Here, the product is called as the ZnO + In + CdSe hetero-nanostructure. If the CdSe QDs are directly deposited onto the ZnO NWs, the product is called as the ZnO@CdSe hetero-nanostructure. (4) ZnO@γ-In_2Se_3 hetero-nanostructures: ZnO@γ-In_2Se_3 hetero-nanostructures were synthesized by annealing the ZnO + In + CdSe hetero-nanostructures under vacuum at 350 °C for one hour.

Characterization

The morphologies of the prepared nanostructures were confirmed by a field-emission scanning electron microscope (FE-SEM, XL30S, Philips) operated at 5.0 kV beam energy and a high-resolution scanning transmission electron microscope (HR-STEM; JEM-2200FS with Image Cs-corrector; JEOL) operated at 200 kV beam energy. Electron energy loss spectroscopy (EELS) data were taken using the three-window method. The crystalline structures were observed by fast Fourier transform (FFT) patterns of transmission electron microscopy (TEM) and X-ray diffraction (XRD, D/MAX-2500, Rigaku) with Cu Kα radiation (40 kV, 100 mA). The XRD spectra were measured in the range of 20°–80° with a scan rate of 4° min^{-1}. To prepare the samples for TEM, the samples were exfoliated from the substrate and dispersed in ethanol using an ultrasonicator. The dispersed samples were deposited on a copper grid and were placed in an electrical oven for 1 day to remove the ethanol.

PEC and photocatalytic tests

The optical absorbance of the samples was analyzed using a UV2501PC (SHIMADZU) spectrometer with an ISR-2200 integrating sphere attachment for diffuse reflection measurement. The photocurrent–voltage (*I–V*) measurements were performed using a typical three-electrode potentiostat system (Potentiostat/Galvanostat, model 263A, EG&G Princeton Applied Research) with a Pt counter electrode and a saturated calomel reference electrode (SCE). The electrolyte was an aqueous solution of 0.25 M Na_2S and 0.35 M Na_2SO_3 through which nitrogen was bubbled. The working electrode was illuminated from the front side with a solar-simulated light source (AM 1.5 G filtered, 100 mW cm^{-2}, 91160, Oriel).

To examine the photocatalytic activity, acid orange 7 (AO7) was chosen as a probe molecule because of its resistance to biological degradation. The evaluation of the photocatalytic activity of the prepared samples for the photocatalytic decolorization of AO7 aqueous solution was performed at room temperature. All the samples were cut into 1 × 3 cm^2 and were immersed into 20 ml of AO7 aqueous solution (1×10^{-5} M). For the UV light test, the samples were irradiated using a UV lamp with a wavelength of 312 nm (LF-215 LM, 230 V, 30 W, UVITEC, model 06-12782). For the sunlight test, the samples were irradiated using a Xenon lamp (300 W, Oriel, model 66902) directed towards the center of the sample in a closed system. A water filter was mounted on the lamp housing to eliminate infrared radiation (IR) and a cutoff filter was placed outside the light slit of the lamp for the complete removal of radiation below 400 nm to ensure that photocatalysis is achieved by visible light irradiation only. Prior to irradiation, the AO7 aqueous solution was vigorously stirred at room temperature and kept in the dark. After irradiation, the reaction solution was separated to measure the change in the concentration of AO7. The cut-on wavelength for the long pass filter is 700 nm (FEL0700, Thorlabs Inc).

Results and discussion

Morphologies and reaction mechanism

The four step synthesis route to the ZnO@γ-In_2Se_3 hetero-nanostructures (HNSs) and their corresponding morphologies are shown in Fig. 1a and b–e, respectively. First, large-area ZnO NWs are closely erected on the FTO substrate *via* a hydrothermal method (Fig. 1b). The enlarged view of the inset exhibits that the diameter of a single ZnO NW is about 200 nm. In order to avoid confusion in the following, this structure is called as "Bare ZnO NWs". Then, a thin In layer is coated on the surface of the ZnO NW using RF magnetron sputtering for 30 seconds (Fig. 1c). The ZnO NW with coated In layer has a diameter of 300 nm and is called as "In-coated ZnO NWs". Third, the CdSe QDs are deposited on the In layer using chemical bath deposition (Fig. 1d). The product is called as "ZnO + In + CdSe HNS". Finally, the CdSe QDs are converted into γ-In_2Se_3 QDs by annealing under vacuum at 350 °C for one hour, and the element Cd is sublimed. The SEM image in Fig. 1e shows that the γ-In_2Se_3 QDs with uniform sizes are closely adhered to the surface of the ZnO NW, which makes the diameter of the ZnO NW increase to nearly 500 nm. During the synthesis process, the conversion of the ZnO + In + CdSe HNS to the ZnO@γ-In_2Se_3 HNSs is the most crucial point. Thus, TEM and the energy dispersive X-ray spectroscopy (EDS) observations were performed to analyze the crystalline structures and constituent elements step by step. The In-coated ZnO NW in Fig. 2a demonstrates that the In layer is entirely covered on the surface of the ZnO NW. Taken from the high resolution TEM (HRTEM) image in Fig. 2b, the lattice fringe spacing of 0.26, 0.25 and 0.29 nm correspond to the (002) face of ZnO, (100) face of In and (222) face of In_2O_3. The element mapping of Fig. 2c reconfirms that the In atoms are uniformly distributed outside the ZnO NW. After the deposition of CdSe, the CdSe QDs with the diameters of ~50 nm are prominent on the surface of the In-coated ZnO NW (Fig. 2d). The HRTEM image in Fig. 2e shows that the CdSe QDs are a single crystalline structure with a fringe spacing of 0.36 nm corresponding to its (111) face.[22] The element mapping in Fig. 2f shows that the In layer is retained and that the Cd and Se elements are evenly distributed.

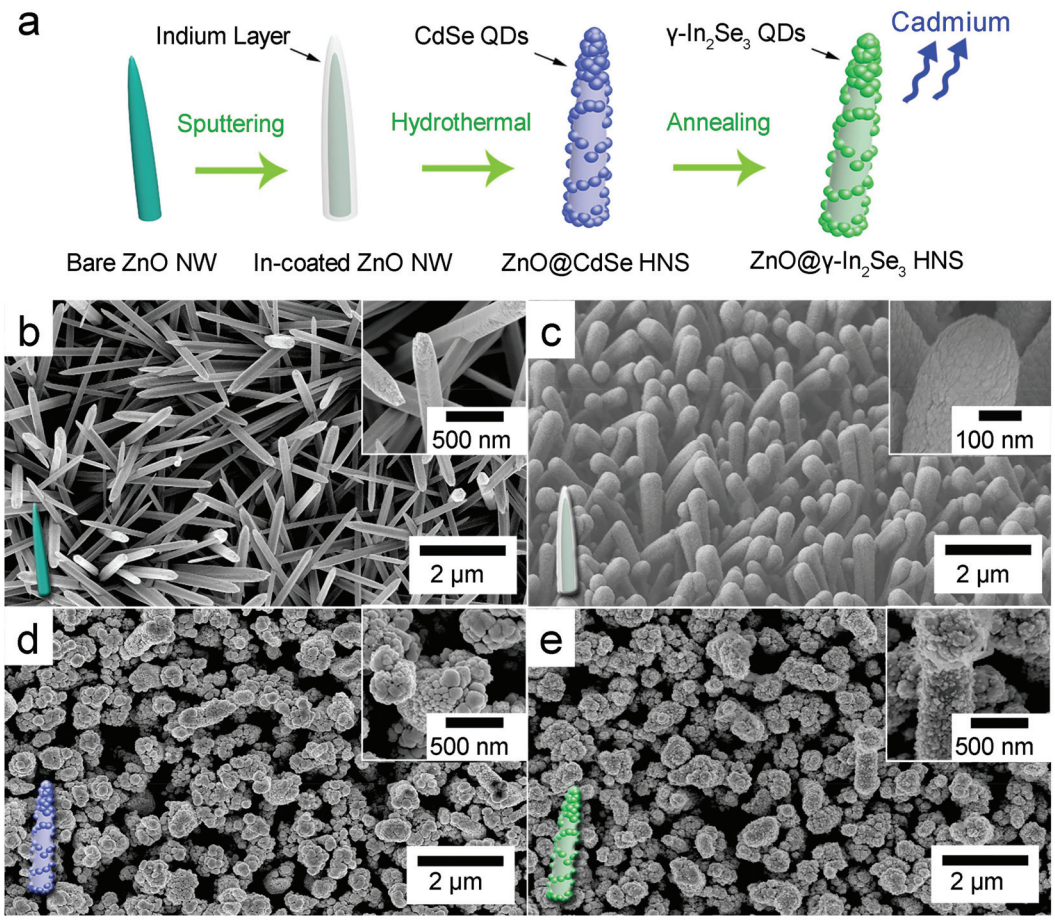

Fig. 1 (a) Synthetic route to the ZnO@γ-In_2Se_3 HNS; (b–e) top-view SEM images of bare ZnO NWs (b), In-coated ZnO NWs (c), ZnO + In + CdSe HNSs (d) and ZnO@γ-In_2Se_3 HNSs (e). The insets on the upper right are the corresponding enlarged views, whereas the insets on the bottom left are their sketches.

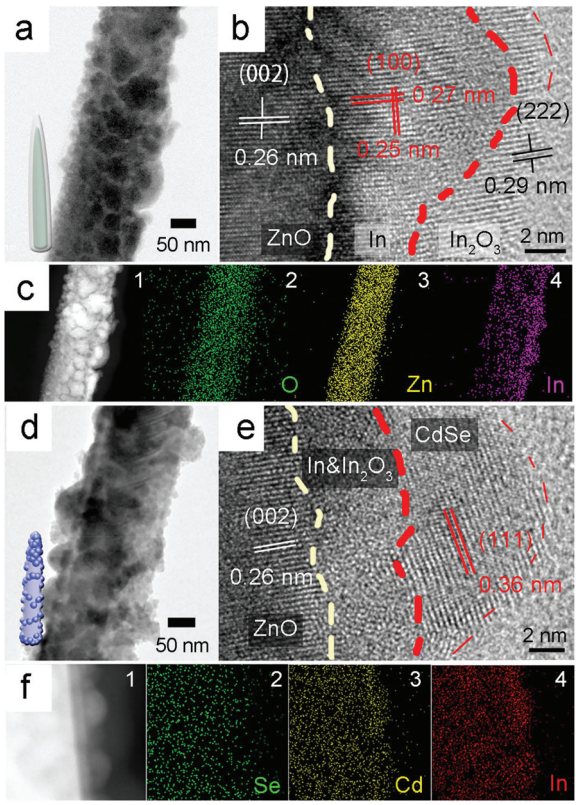

Fig. 2 (a) TEM image of a single In-coated ZnO NW; (b) HRTEM image of the In-coated ZnO NW; (c) annular dark field (ADF) image (1) of the In-coated ZnO NW and the corresponding EDS elemental mapping of O (2), Zn (3) and In (4); (d) TEM image of a single ZnO + In + CdSe HNS; (e) HRTEM image of the ZnO + In + CdSe HNS; (f) ADF image (1) of the ZnO + In + CdSe HNS and the corresponding EDS elemental mapping of Se (2), Cd (3) and In (4).

After annealing under vacuum at 350 °C for one hour, the γ-In_2Se_3 QDs are generated and evenly distributed on the surface of the ZnO NW (Fig. 3a). It can be seen that the γ-In_2Se_3 QDs have sizes ranging from 20 to 70 nm. Between the ZnO NW (region 1, white color) and the γ-In_2Se_3 QD (region 3, green color), there is a very thin layer of In_2O_3 (region 2, yellow color), as shown in Fig. 3b. In addition, both the ZnO NW (Fig. 3c) and the In_2O_3 layer are single crystal structures (the inset of Fig. 3c). Fig. 3d exhibits that the γ-In_2Se_3 QD is a single crystalline structure and has the fringe spacing of 0.29 nm, which corresponds to the (202) face of hexagonal γ-In_2Se_3.[23] Furthermore, the FFT pattern with the diffraction spots of (111), (112) and (220), as shown in the inset of Fig. 3d, also demonstrates its hexagonal structure. To check the content and distribution of Cd atoms, spatial elemental analysis using electron energy loss spectroscopy (EELS) was employed, and the elemental mapping is shown in Fig. 3e. It can be seen that the EELS mapping of the Cd signal in the background is stronger than in the region of the ZnO NW under the higher signal-to-noise ratio, which demonstrates that the Cd content is lower than noise. Thus, it confirms that Cd atoms are totally eliminated. Comparatively, both the elements In and Se are evenly distributed on the surface of the ZnO NW. Moreover, Zn and O are only found in the ZnO NW region. Based on the analysis using TEM and EELS, it is confirmed that the conversion products are γ-In_2Se_3 QDs and the Cd atoms in CdSe QDs were totally replaced with In.

For better understanding of the mechanism for the conversion of CdSe QDs to γ-In_2Se_3 QDs, the effect of the conversion temperature on the product composition was explored. First, 24 samples of the ZnO + In + CdSe HNSs were prepared and every 2 samples were annealed at the same temperature for getting the average value of the element amounts. The anneal-

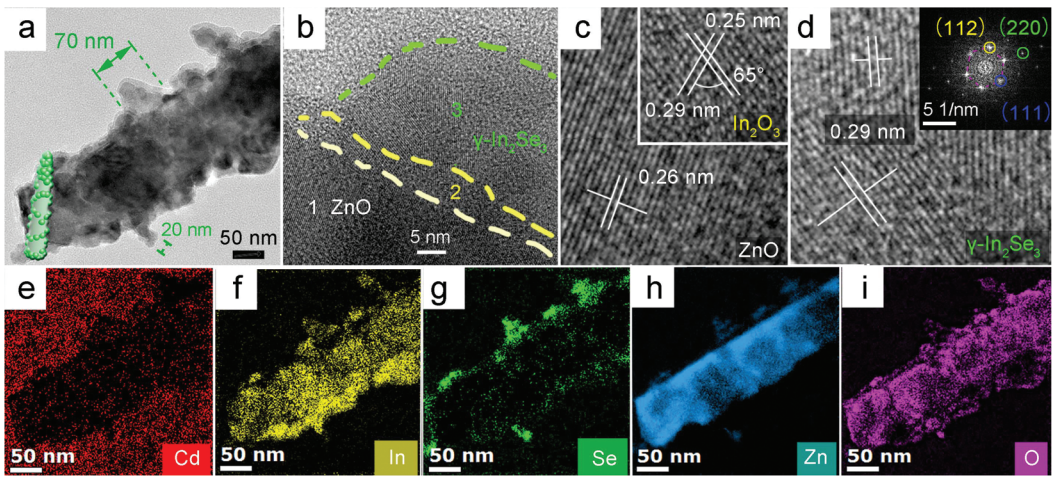

Fig. 3 (a, b) TEM (a) and HRTEM (b) images of a single ZnO@γ-In_2Se_3 HNS; (c, d) lattice fringes taken from region 1 (c) and 3 (d) of (b). The inset of (c) is the lattice fringes taken from region 2, and the inset of (d) is the corresponding FFT patterns for region 3; (e–i) element mapping of Cd (e), In (f), Se (g), Zn (h) and O (i) for the ZnO@γ-In_2Se_3 HNS using EELS.

ing temperatures were increased from 95 °C to 400 °C at intervals of 25 °C. The elemental ratios of each component over Zn atoms were investigated because the amount of the Zn atoms in each sample is thought to remain constant below 400 °C due to the melting point of nearly 750 °C for nano-sized ZnO.[24] Thus, if the atomic percentage of Cd and Zn in one sample is 24% and 6% using EDS analysis, respectively, the ratio Cd/Zn = 0.25 can serve as the relative amount of Cd in the sample. Then, the relative amounts of the Cd, Se and In in an area of 20 × 20 μm^2 for all the samples were exploited together to constitute the trend of the compositional changes in the ZnO + In + CdSe HNSs upon increasing the annealing temperature (Fig. 4a). Fig. 4a shows that from 95 °C to 175 °C the amount of Cd and In decreases significantly. It is ascribed to the sublimation of Cd and In, which have a melting point of only 150–175 °C[25] and 110 °C[26] for nanostructures, respectively. Below 175 °C, Se has changed slightly due to its higher melting point of 220 °C for nanostructures.[27] Next, due to the different initial amounts of each element in each sample, the amount of Se, Cd and In atoms show fluctuations from 0.08 to 0.25 with increasing annealing temperatures from 175 °C, whereas Cd is eliminated by evaporation above 350 °C, and both Se and In are eliminated by evaporation above 375 °C. The drastic decrease in Cd composition to zero at 350 °C suggests that the conversion of CdSe into InSe is completed at this temperature.

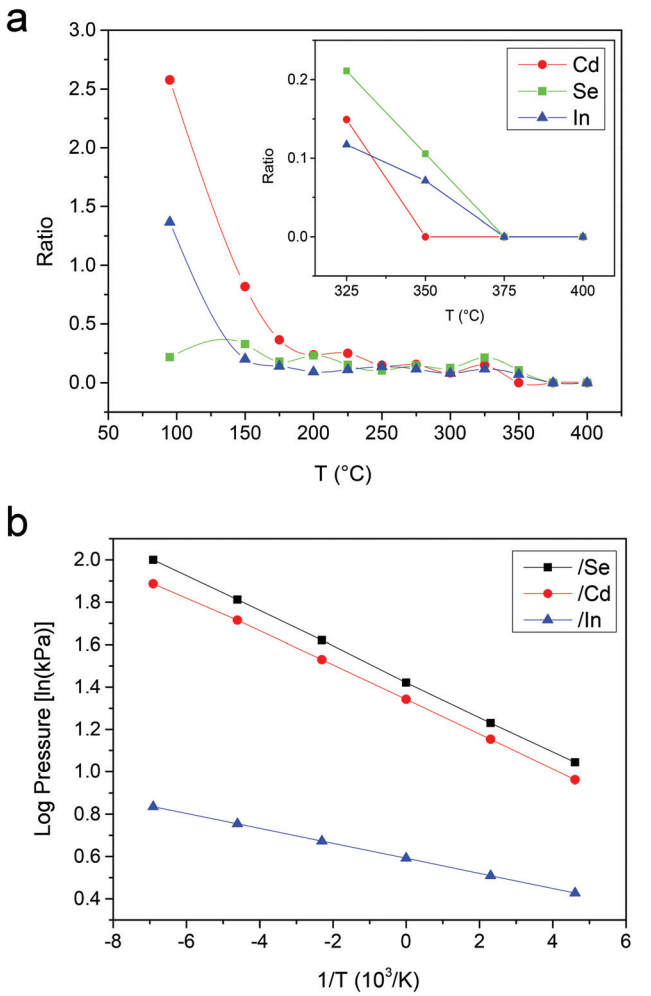

Fig. 4 (a) Ratios of the atomic amounts of Cd, Se and In to Zn with increasing annealing temperatures. The inset is the enlarged view from 325 °C to 400 °C; (b) the log pressure curves for Se, Cd and In.

Using the differential scanning calorimetry (DSC) method, M. F. Kotkata reported that the CdSe nanoparticles had a melting point ranging from 530 °C to 870 °C with an increase in size from several nanometers to bulk-size.[28] M. P. Das also demonstrated that the melting point of nano-sized CdSe was 700 K (≈426 °C),[29] yet the phase transition from the CdSe zinc blende structure to the wurtzite structure occurs at 310–330 °C.[28] Thus, In in the molten state and Se in the CdSe QDs can easily combine into indium selenide (In_xSe_y) above 310 °C due to the structural instability of CdSe. Moreover, the melting point of 680 °C for nano-sized In_xSe_y is higher than that of CdSe.[30] Therefore, in the temperature range between 310 °C and 350 °C, the element Cd in CdSe QDs is gradually replaced with In. Above 375 °C, both the elements Se and In are also eliminated (inset of Fig. 4a) due to the ongoing sublimation and vacuum-pumping. Thus, the best temperature for replacing the element Cd in CdSe QDs with In is 350 °C.

Then, to understand the mechanism of this thermal chemical reaction, we checked the saturated vapor pressures of Se, Cd and In,[31] and plotted their log pressure curves in Fig. 4b. It is well known that, with increasing temperature, the molecular kinetic energy becomes higher, and then more molecules can escape from the surface and the saturated vapor pressure is correspondingly higher. Thus, the higher the saturated vapor pressure an element has, the easier this element can evaporate. In this thermal chemical reaction, 350 °C is far above the melting points of In and close to that of the nano-sized CdSe (426 °C).[29] Although the In layer is melted, In has a lower saturated vapor pressure than Cd and Se (Fig. 4c). Thus, Cd is easier to evaporate than In and the Cd vapor is eliminated in the vacuum system.

To further confirm the elimination of CdSe and the formation of γ-In_2Se_3 after annealing, the ZnO + In + CdSe HNSs before and after annealing were compared using XRD analysis (Fig. 5a). The results show that three evident peaks for CdSe at (111), (220) and (331) are present in the ZnO + In + CdSe HNSs before annealing. Here, InS peaks are observed before annealing, which is ascribed to the reaction between the In layer and SO_3^{2-} in the electrolyte. In addition, In peaks do not appear and coincide with the HRTEM image of Fig. 2e. After annealing, the CdSe peaks disappear, whereas hexagonal γ-In_2Se_3 peaks for (112), (202) and (116) are detected. Moreover, single-crystal In_2O_3 is present due to the oxidation of In layer at high temperature, which is consistent with the TEM observations shown in Fig. 3b and c. Moreover, the SnO_2 peaks are evident both before and after annealing, which is ascribed to the FTO glass substrate. It is noticed that the CdSe peaks are lower and wider than those for γ-In_2Se_3. According to the Scherrer equation, the size of sub-micrometer particles or crystallites in

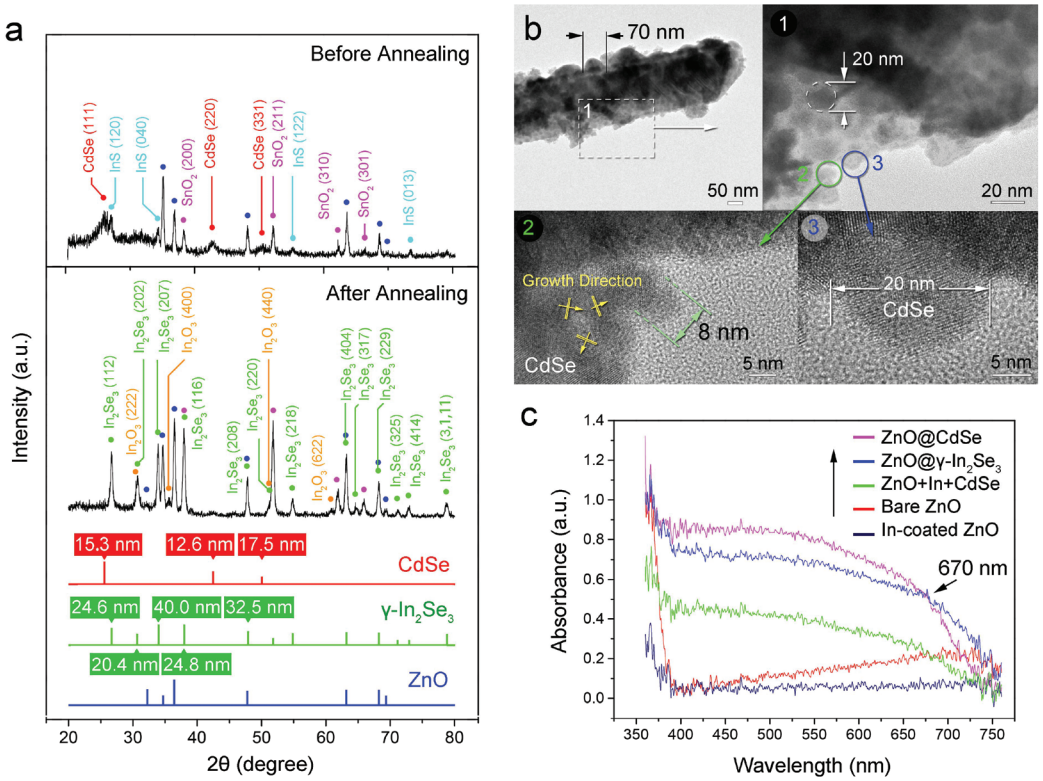

Fig. 5 (a) XRD patterns for the ZnO + In + CdSe HNSs (before annealing) and ZnO@γ-In_2Se_3 HNSs (after annealing). The diffraction peaks for CdSe, γ-In_2Se_3, ZnO, InS, SnO_2 and In_2O_3 are distinguished by red, green, blue, wathet, purple and orange, respectively. The standard spectra for CdSe, γ-In_2Se_3 and ZnO are listed at the bottom. The sizes of crystallites are labeled on the corresponding diffraction peaks; (b) TEM image of the ZnO + In + CdSe nanorod. Fig. b1 is the enlarged-view of Fig. b. Fig. b2 and b3 are the HRTEM images taken from the marked regions in Fig. b1; (c) the absorption spectra for ZnO@CdSe HNSs, ZnO@γ-In_2Se_3 HNSs, ZnO + In + CdSe HNSs, bare ZnO NWs and In-coated ZnO NWs.

a solid is related with the broadening of a peak in the diffraction pattern. Then, the sizes of the CdSe and γ-In_2Se_3 crystallites were calculated and marked on the corresponding peaks shown in the bottom of Fig. 5a. The CdSe QDs have crystallite sizes ranging from 10 to 20 nm (red color), whereas γ-In_2Se_3 has bigger crystallites ranging from 20 to 40 nm (green color). Although the TEM image of the ZnO + In + CdSe nanorod, as exhibited in Fig. 5b, shows that some CdSe nanoparticles are bigger than 70 nm, there are still many small CdSe QDs distributed on the surface of the nanorod. For instance, the crystallite sizes of the CdSe QDs, as shown in region 1, 2 and 3, have small sizes of 8–20 nm, which is similar to the calculated size from XRD. Moreover, Fig. 5 b2 shows that bigger CdSe nanoparticles can be assembled by small single crystal regions with different growth directions (marked with yellow arrows). Therefore, the γ-In_2Se_3 QDs generated have larger sizes, but smaller size ranges than CdSe QDs. It is because most CdSe QDs smaller than 20 nm are sublimed after annealing.

The EDS and XRD results demonstrate that annealing at 350 °C efficiently drives the conversion of CdSe to γ-In_2Se_3 and that this is absolutely a thermal chemical reaction. Therefore, the main driving force of this thermal reaction includes not only the higher melting point of γ-In_2Se_3 than that of nano-sized CdSe, but also the different saturated vapor pressures of Se, Cd and In. Furthermore, indium selenide (In_xSe_y) has various crystal structures such as hexagonal α(2*H*)-In_2Se_3, rhombohedral β(3*R*)-In_2Se_3, hexagonal γ-In_2Se_3 and orthorhombic In_4Se_3. Between them, only hexagonal γ-In_2Se_3 can be formed by heating β(3*R*)-In_2Se_3 at 350 °C.[15] It is also consistent with the XRD analysis. The reaction equation can be written as follows:

$$2In + 3CdSe \xrightarrow{350\ ^\circ C,\ in\ vacuum} \gamma - In_2Se_3 + 3Cd\uparrow$$

Photoelectrochemical and photocatalytic performances

To evaluate the capability of light absorption for photoelectrochemical (PEC) and photocatalytic applications, the optical absorption spectra of the five samples, ZnO@CdSe HNSs, ZnO@γ-In_2Se_3 HNSs, ZnO + In + CdSe HNSs, bare ZnO NWs and In-coated ZnO NWs, were measured (Fig. 5c). Here for comparison, we deposited the CdSe QDs directly onto the bare ZnO NWs and called this nanostructure as "ZnO@CdSe hetero-nanostructures (HNSs)". The spectra curves show that the bare ZnO NW arrays absorb only in the UV region at wavelengths up to 400 nm. The ZnO@CdSe HNSs, ZnO@γ-In_2Se_3 HNSs and ZnO + In + CdSe HNSs extend the absorption range to the whole visible spectrum. Although ZnO@CdSe HNSs exhibit the strongest capacity of light absorption from 400 nm

to 670 nm due to the smaller single crystalline sizes, the absorption turns stronger for the ZnO@γ-In_2Se_3 HNSs than the ZnO@CdSe HNSs for longer wavelengths over 670 nm. The red-shift is mainly caused by the lower band gap (<1.7 eV) and the larger size of the γ-In_2Se_3 QDs when compared to CdSe QDs.

The photoelectrochemical (PEC) properties of the prepared ZnO@γ-In_2Se_3 HNSs photo-anodes were characterized using a three-electrode PEC system. Fig. 6a is a schematic diagram of the ZnO@γ-In_2Se_3 PEC cell with sacrificial reagent electrolytes and the mechanism of hydrogen generation in our system. Under irradiation, photo-generated electrons in the narrow band gap semiconductor γ-In_2Se_3 are injected into the conduction band of ZnO, whereas the remaining holes in the cathode oxidize the S^{2-} ions into S_2^{2-} ions, and the conductive In_2O_3 is employed as the bond connecting ZnO with γ-In_2Se_3. Through the multi-level band position of the electrodes, electrons pass through γ-In_2Se_3 to the FTO substrate and transfer to the Pt counter electrode. The electrons at the Pt counter electrode are consumed to reduce H^+ to H_2. The role of the sacrificial reagent in the electrolyte (SO_3^{2-}) is to prevent a back reaction of reducing S_2^{2-} to S^{2-}.[32] This figure explains the mechanism for PEC hydrogen generation in our system.

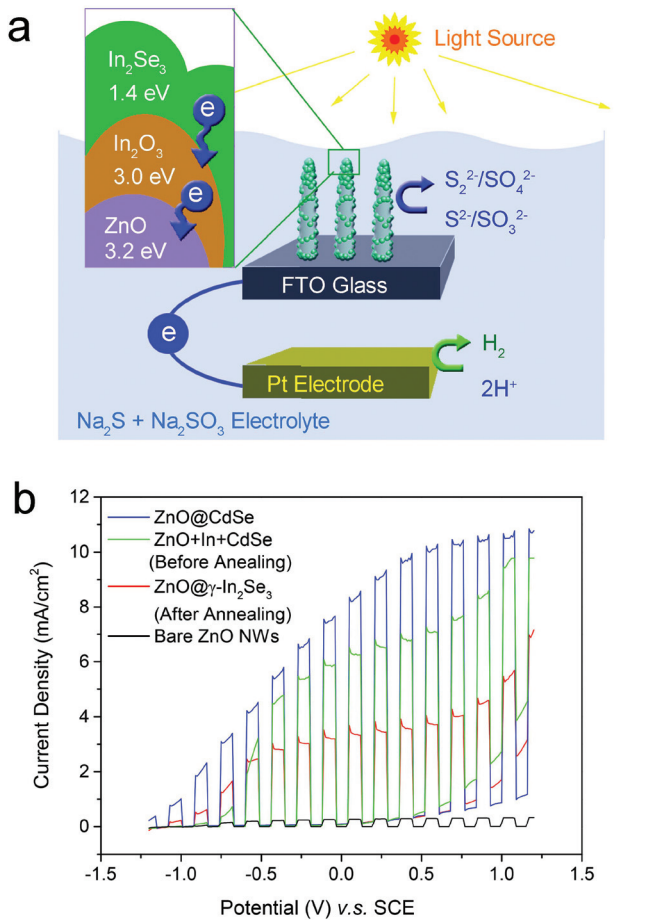

Fig. 6 (a) Schematic diagram showing the PEC cell based on the ZnO@γ-In_2Se_3 HNSs and the charge-transfer processes; (b) chopped illumination (100 mW cm^{-2}) current density *versus* potential (*J*–*E*) characteristics for the ZnO@CdSe HNSs, ZnO@γ-In_2Se_3 HNSs with different thicknesses, ZnO + In + CdSe HNSs and bare ZnO NWs.

Fig. 6b is a set of chopped sweep current density *versus* potential curves obtained from the photoanodes of ZnO@CdSe HNSs, ZnO@γ-In_2Se_3 HNSs, ZnO + In + CdSe HNSs and bare ZnO NWs using a white light illumination of 100 mW cm^{-2} (AM 1.5 G). Here, In-coated ZnO NWs are not included because In is a good conductor of electricity. As expected from the optical absorption spectra, the ZnO@CdSe HNSs have the lowest open-circuit voltage (V_{oc}) far below −1.2 eV *versus* a saturated calomel reference electrode (SCE) and the strongest current density. Comparatively, ZnO@γ-In_2Se_3 HNSs have a V_{oc} of about −1.1 eV, and the current density of which is only half of the ZnO@CdSe HNSs. This is because small CdSe QDs are eliminated after annealing and then only γ-In_2Se_3 QDs having large sizes can be formed. Furthermore, the partial sintering or fused state of the γ-In_2Se_3 QDs can reduce the exposed surfaces, which is also disadvantageous to PEC performance. Similarly, the current density of ZnO + In + CdSe HNSs is also higher than ZnO@γ-In_2Se_3 HNSs due to the large amount of QD loading. The V_{oc} of ZnO + In + CdSe HNSs is only about −0.75 eV, which is ascribed to the conductive In layer. Here, we notice that the ZnO@γ-In_2Se_3 HNSs and ZnO + In + CdSe HNSs have evident dark current, which may be ascribed to the conductive In_2O_3 layer that cannot be fully covered by the γ-In_2Se_3 QDs. The In_2O_3 layer has good conductivity and is difficult to solubilize in acids. Thus, it has two important functions here: (1) connecting the ZnO with γ-In_2Se_3 with lower resistivity; (2) covering ZnO and preventing ZnO from being dissolved in PEC electrolyte. Among all of the samples, the bare ZnO NWs have the weakest PEC performance due to its effective absorption being confined to the UV region.

In addition to the current density, stability is also very important for PEC capability. The PEC stabilities of the ZnO@γ-In_2Se_3 HNSs and ZnO@CdSe HNSs were tested and are shown in Fig. 7a. After being tested six times, the current density drop of the ZnO@γ-In_2Se_3 HNSs was less than that of the ZnO@CdSe HNSs. To clearly show this comparison, the current densities generated at the potential of 1.05 V were taken and plotted, as shown in Fig. 7b. Comparison analysis shows that the current density of the ZnO@γ-In_2Se_3 HNSs decreases by only 0.57 mA cm^{-2} after six tests, whereas the decreased value of the ZnO@CdSe HNSs is 1.85 mA cm^{-2}. By calculation, the current density of the ZnO@γ-In_2Se_3 HNSs decreases about 10%, yet the ZnO@CdSe HNSs decreases by nearly 20%. Therefore, our prepared ZnO@γ-In_2Se_3 HNSs have lower but more stable photo-current density than ZnO@CdSe HNSs. The good stability is ascribed to the protection of the In_2O_3 layer between the ZnO NW and the γ-In_2Se_3 QDs. Because In_2O_3 is not dissolved in water and is non-reactive to acid,[33] the In_2O_3 layer prevents the ZnO NW from dissolving in the PEC weak-acid solution and blocks the detachment of the γ-In_2Se_3 QDs from the ZnO NW.

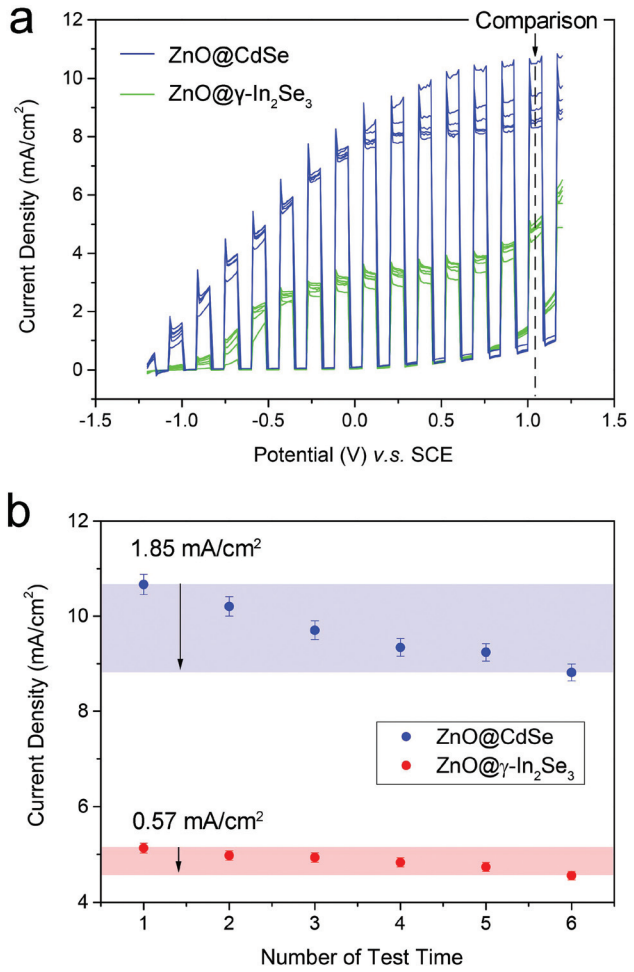

Fig. 7 (a) Comparison *J–E* curves under chopped illumination with ZnO@CdSe HNSs and thicker ZnO@γ-In_2Se_3 HNSs tested six times; (b) current densities for ZnO@CdSe HNSs and ZnO@γ-In_2Se_3 HNSs tested under 1.05 V six times. Error bars exhibit the deviation of experimental accuracy.

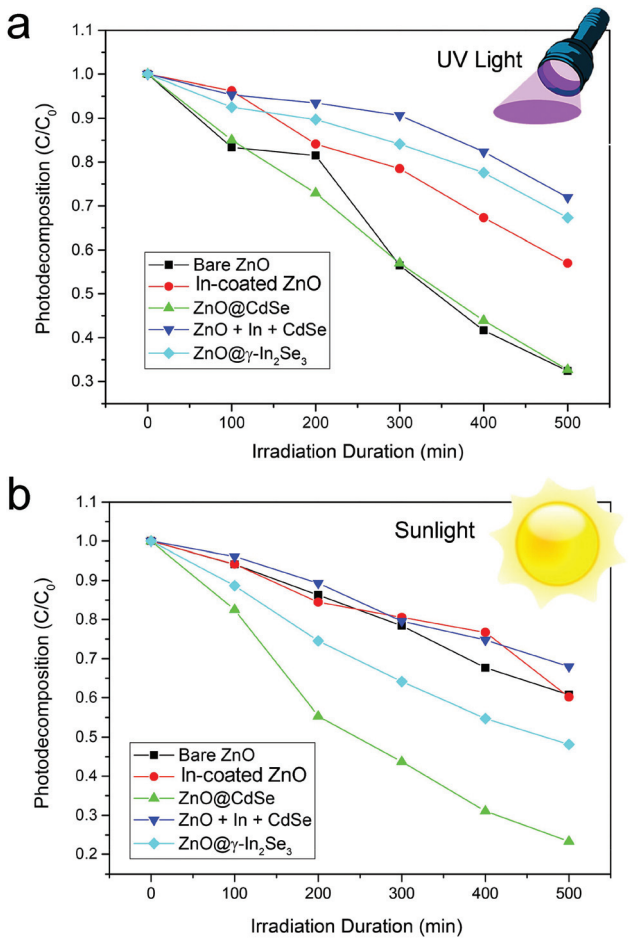

Fig. 8 (a, b) Comparison of the photocatalytic activities of bare ZnO NWs, In-coated ZnO NWs, ZnO@CdSe HNSs, ZnO + In + CdSe HNSs and ZnO@γ-In_2Se_3 HNSs for the photocatalytic decolorization of AO7 in water irradiated with UV light (a) and sunlight (b).

For further understanding the photo-applications of our prepared ZnO@γ-In_2Se_3 HNSs, the photocatalytic performances were also tested. Here for comparison, five samples of ZnO@CdSe HNSs, ZnO@γ-In_2Se_3 HNSs, ZnO + In + CdSe HNSs, bare ZnO NWs and In-coated ZnO NWs, were tested using AO7 solutions. Considering that the effective absorption wavelength of the bare ZnO NWs is less than 400 nm and the ZnO@γ-In_2Se_3 HNSs exhibits stronger absorption than ZnO@CdSe HNSs in the wavelength longer than 670 nm, we firstly tested the photocatalytic performances of the five samples in the UV region, then in sunlight with all wavelengths, and finally in the wavelength region beyond 700 nm. Fig. 8a shows the photocatalytic activities of the five samples tested in UV light at 375 nm. The ZnO@CdSe HNSs and bare ZnO NWs exhibit higher enhanced photocatalytic activity when compared with the other samples due to the enhanced UV light absorption and cascade band structure of CdSe/ZnO. For the photocatalytic test in sunlight (Fig. 8b), bare ZnO NW photocatalysts showed highly decreased photocatalytic activity when compared to the UV case due to its wide band gap of 3.2 eV. Comparatively, ZnO@CdSe HNSs and ZnO@γ-In_2Se_3 HNSs showed significantly enhanced photocatalytic activity when compared to those of the ZnO + In + CdSe HNSs, In-coated ZnO NWs and bare ZnO NWs. The enhancement mainly comes from the suitable band gap of γ-In_2Se_3 (1.7 eV) and CdSe (1.7 eV) and their cascade band structures with ZnO.[34] The photocatalytic activity of the ZnO@γ-In_2Se_3 HNSs is slightly weaker due to the sublimation of the smaller QDs after annealing, as well as the partial sintering or fused state of the γ-In_2Se_3 QDs. Finally, a long pass filter with a cut-off edge at 700 nm was used for the test using wavelengths beyond 670 nm. The beam path and the transmission parameters of the long pass filter are shown in Fig. 9a and its inset. It can be seen that only light having a wavelength beyond 700 nm can pass through into the bottle, which is filled with AO7 solution and has a piece of sample in it. The photocatalytic activity of the ZnO@γ-In_2Se_3 HNSs is better than that of ZnO@CdSe HNSs in the wavelength region

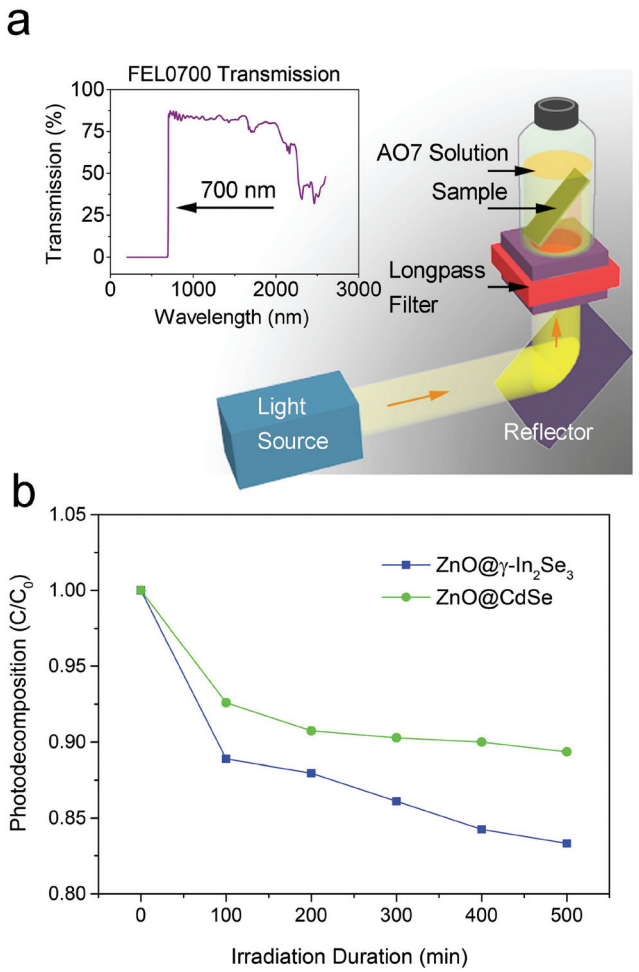

Fig. 9 (a) The sketch of the beam path in the photocatalytic test. The inset is the transmission parameter of the 700 nm long pass filter; (b) comparison of the photocatalytic activities of ZnO@CdSe HNSs and ZnO@γ-In_2Se_3 HNSs for the photocatalytic decolorization of AO7 in water irradiated with light having wavelength beyond 700 nm.

beyond 700 nm (Fig. 9b). The result confirms that our prepared ZnO@γ-In_2Se_3 HNSs exhibit enhanced photocatalytic activity in a wider wavelength region from 400 nm to almost 750 nm, suggesting ZnO@γ-In_2Se_3 HNSs as a promising photocatalyst in the near IR region.

Conclusions

Using the thermal characteristics of Cd, which have a higher saturated vapor pressure than In, we have successfully prepared the ZnO@γ-In_2Se_3 hetero-nanostructures on FTO glass by replacing Cd with In for the first time. This thermal replacement reaction is performed by annealing Zn + In + CdSe hetero-nanostructures under vacuum at 350 °C for one hour. The prepared ZnO@γ-In_2Se_3 hetero-nanostructures generated high PEC photocurrents with good stability with the aid of the protection of In_2O_3 layer. The photocatalytic activity is also well demonstrated with effective absorption of light over a wide wavelength region from 400 nm to nearly 750 nm. The prepared ZnO@γ-In_2Se_3 hetero-nanostructures have high potential as efficient photocatalysts in eco-friendly photo-applications. Our newly developed thermal replacement reaction is also applicable to the preparation of other QDs, which cannot be realized using a typical replacement reaction.

Acknowledgements

This work is supported by the National Research Foundation (NRF) of Korea under grant no. 2013-R1A2A2A05-005344.

Notes and references

1 M. S. Yavuz, Y. Y. Cheng, J. Y. Chen, C. M. Cobley, Q. Zhang, M. Rycenga, J. W. Xie, C. Kim, K. H. Song, A. G. Schwartz, L. V. Wang and Y. N. Xia, *Nat. Mater.*, 2009, **8**, 935.
2 S. E. Skrabalak, L. Au, X. D. Li and Y. N. Xia, *Nat. Protocols*, 2007, **2**, 2182.
3 Y. G. Sun and Y. N. Xia, *J. Am. Chem. Soc.*, 2004, **126**, 3892.
4 J. Y. Chen, B. Wiley, J. McLellan, Y. J. Xiong, Z. Y. Li and Y. N. Xia, *Nano Lett.*, 2005, **5**, 2058.
5 V. N. Soloviev, A. Eichhöfer, D. Fenske and U. Banin, *J. Am. Chem. Soc.*, 2000, **122**, 2673.
6 M. Seol, H. Kim, W. Kim and K. Yong, *Electrochem. Commun.*, 2010, **12**, 1416.
7 E. Elmalem, A. E. Saunders, R. Costi, A. Salant and U. Banin, *Adv. Mater.*, 2008, **20**, 4312.
8 Y. Choi, M. Seol, W. Kim and K. Yong, *J. Phys. Chem. C*, 2014, **118**, 5664.
9 C. D. Foy, R. L. Chaney and M. C. White, *Annu. Rev. Plant Physiol.*, 1978, **29**, 511.
10 S. Emin, S. P. Singh, L. Han, N. Satoh and A. Islam, *Solar Energy*, 2011, **85**, 1264.
11 S. Emin, M. Fanetti, F. F. Abdi, D. Lisjak, M. Valant, R. van de Krol and B. Dam, *ACS Appl. Mater. Interfaces*, 2013, **5**, 1113.
12 B. Pejova and I. Grozdanov, *J. Solid State Chem.*, 2001, **158**, 49.
13 W. D. Luo, S. Ismail-Beigi, M. L. Cohen and S. G. Louie, *Phys. Rev. B: Condens. Matter*, 2002, **66**, 195215.
14 P. K. Khanna and B. K. Das, *Mater. Lett.*, 2004, **58**, 1030.
15 G. Han, Z. G. Chen, J. Drennan and J. Zou, *Small*, 2014, **10**, 2747.
16 D. Wei, Z. G. Lin, Z. T. Cui, S. Y. Su, D. K. Zhang, M. H. Cao and C. W. Hu, *Chem. Commun.*, 2013, **49**, 9609.
17 R. Sreekumar, R. Jayakrishnan, C. S. Kartha and K. P. Vijayakumar, *J. Appl. Phys.*, 2006, **100**, 033707.
18 H. Peng, D. T. Schoen, S. Meister, X. F. Zhang and Y. Cui, *J. Am. Chem. Soc.*, 2007, **129**, 34.
19 T. Y. Zhai, X. S. Fang, M. Y. Liao, X. J. Xu, L. Li, B. Liu, Y. Koide, Y. Ma, J. N. Yao, Y. Bando and D. Golberg, *ACS Nano*, 2010, **4**, 1596.

20 T. Okamoto, Y. Nakada, T. Aoki, Y. Takaba, A. Yamada and M. Konagai, *Phys. Status Solidi C*, 2006, **3**, 2796.
21 R. Vaidyanathan, J. L. Stickney, S. M. Cox, S. P. Compton and U. Happek, *J. Electroanal. Chem.*, 2003, **559**, 55.
22 H. Kim, M. Seol, J. Lee and K. Yong, *J. Phys. Chem. C*, 2011, **115**, 25429.
23 H. D. Lutz, M. Fischer, H.-P. Baldus and R. Blachnik, *J. Less-Common Met.*, 1988, **143**, 83.
24 X. Su, Z. J. Zhang and M. M. Zhu, *Appl. Phys. Lett.*, 2006, **88**, 061913.
25 P. Mohanty, J. Park, G. Lee and B. Kim, *J. Nanosci. Nanotechnol.*, 2006, **6**, 1.
26 S. Cingarapu, Z. Q. Yang, C. M. Sorensen and K. J. Klabunde, *Inorg. Chem.*, 2011, **50**, 5000.
27 Z. X. Chen, Y. H. Shen, A. J. Xie, J. M. Zhu, Z. F. Wu and F. Z. Huang, *Cryst. Growth Des.*, 2009, **9**, 1327.
28 M. F. Kotkata, A. E. Masoud, M. B. Mohamed and E. A. Mahmoud, *Physica E*, 2009, **41**, 640.
29 M. P. Das, *Adv. Nat. Sci.: Nanosci. Nanotechnol.*, 2010, **1**, 043001.
30 X. H. Sun, B. Yu, G. Ng, T. D. Nguyen and M. Meyyappan, *Appl. Phys. Lett.*, 2006, **89**, 233121.
31 See http://en.wikipedia.org/wiki/Vapor_pressures_of_the_elements_(data_page).
32 H. Kim and K. Yong, *ACS Appl. Mater. Interfaces*, 2013, **5**, 13258.
33 S. Barth, M. S. Seifner and J. Bernardi, *J. Mater. Chem. C*, 2014, **2**, 5747.
34 M. Lee and K. Yong, *Nanotechnology*, 2012, **23**, 194014.